Pergamon

Int. J. Heat Mass Transfer. Vol. 41, No. 16, pp. 2537–2548, 1998

Printed in Great Britain
0017-9310/98 $19.00+0.00

PII: S0017-9310(97)00145-2

Visualization study of melting and solidification in convecting hypoeutectic Ga–In alloy

R. DEREBAIL† and J. N. KOSTER‡

Department of Aerospace Engineering Science, University of Colorado, Campus Box 429, Boulder, CO 80309-0429, U.S.A.

(*Received* 12 *August* 1996 *and in final form* 1 *May* 1997)

Abstract—Natural convection flow visualization experiments during melting and solidification of a hypoeutectic gallium five weight percent indium were performed using a real time X-ray radioscopy technique. The experiments revealed a conductive–convective threshold for the onset of natural convection in the alloy. The threshold appears to be caused by a substantial chemical stratification of indium in the melt. The observed gravitational segregation has been evaluated and compared to theoretical models, which, however, do not predict the observations. © 1998 Elsevier Science Ltd. All rights reserved.

1. INTRODUCTION

We consider natural convection in a rectangular cavity. It has been accepted that natural convection develops in differentially heated liquids at any $\Delta T > 0$ K [1]. With a horizontal temperature gradient and a vertical stabilizing concentration gradient, calculations predict thermosolutal convection [2, 3]. The impact of fluid flow on solidification has been recognized: convective flow leads to specific morphologies of the solid–liquid interface [4–8]. Natural convection in low Prandtl number melts was presented by Hurle *et al.* [9]. In a horizontal boat they measured the local temperatures in gallium and mapped the time-dependent character of the flow with thermocouples. Probing with thermocouples and surface motion observations are basic techniques used to get information on low Prandtl number flow [10, 11]. Stewart and Weinberg [12], on the other hand, introduced radioactive tracer materials in liquid tin for visualization purposes.

Chemical segregation in electronic materials and advanced structural alloys is one of the prime foci in materials research. Fundamental segregation issues and the effect of a changing segregation coefficient on the solidification have been reviewed often [13–15]. Observations of unexplained segregation were reported first by Watson [16] in 1932 at the Royal Mint in London for silver–copper alloys. Later, similar phenomena were reported by Allen and Isserow [17], by Reijonen and Forstén [18], and more recently by Glazov [19]. A comprehensive review on indium antimonide research is given by Hulme and Mullin [14] and Mullin [15]. Radioscopic flow visualization revealed substantial chemical segregation in Ga–In alloy melts [20]. No segregation was observed in solidified Pb–Sn eutectics, unless the sample was subjected to high centrifugal forces [21]. It also appears to be technically very difficult to grow bulk Si_xGe_{1-x} single crystals with Czochralski methods because of unexplained segregation [22, 23].

Recently a new, non-invasive, real-time X-ray radioscopy technique has been employed to visualize the morphology of melting and solidifying interfaces [24–26]. The visualization technique is based on the mass absorption of the elements. Mass absorption coefficient values are tabulated in [27] and other handbooks. The X-ray absorption varies as a function of the material density. If the density is changed by temperature, the visualization technique provides temperature field visualization through a variation in the X-ray absorption intensity [28]. In the case of alloys, the visualization provides a combined density and concentration difference visualization. As the absorption coefficient of In is 3.6 times higher than that of Ga and the density of gallium is only weakly dependent on temperature, the radioscopic visualization provides primarily concentration field visualization, and instrument settings are such that the temperature information in the density fields can be neglected. The radioscopic technique is described in more detail in ref. [29]. A description of the X-ray radioscopic facility with a Bridgman–Stockbarger furnace is available in refs. [8, 30, 31].

2. EXPERIMENTAL SETUP

The following work provides flow visualization data of natural convection and chemical segregation in Ga–In alloys which are molten in a horizontal temperature gradient. The composition of the alloy is gallium containing 5% indium, hereafter referred to as Ga–5In

† Currently with Hewlett-Packard Co., San Jose, CA 95131, U.S.A.

‡ Author to whom correspondence should be addressed.

NOMENCLATURE

a	activity coefficients
c_p	specific heat
C	concentration
d	width of cavity
D	diffusion, self-diffusion coefficients
g	gravitational acceleration
Gr	Grashof number
H	height of cavity
I	intensity of X-ray beam after penetration of a material
I_0	intensity of incident X-ray beam
k	thermal conductivity
$K_{\alpha,W}$	characteristic radiation of a tungsten target
l	length of the melt (solid excluded)
L	length of cavity
m	mass
M	mass per mole of solution
O	origin
R	universal gas constant
S	solutal parameter
t	time
T	tempertaure
V, v	volume, small volume
w%	weight percent
x, y, z	coordinates
X_j, X_k	mole friction of components
Z	height.

Greek symbols

β	coefficient of expansion
Δ	difference
κ	thermal diffusivity
μ	dynamic viscosity
$(\mu/\rho)_0$	mass absorption coefficient
ν	kinematic viscosity or momentum diffusivity
ρ	density.

Subscripts

c	cold
Ga	gallium
h	hot
In	indium
j, k	component j, k
liq	liquidus
m	melting
o	initial state
S	solutal
T	thermal
1, 2	components/beam 1 and 2, respectively.

Superscripts

m	melt
s	solid.

for simplicity. The liquidus temperature of the composition is calculated from the phase diagram: $T_{liq} = 25°C$ [32].

The test cell is made of Plexiglas which provides insulating thermal boundary conditions. Molybdenum cladded copper thermodes apply defined thermal boundary conditions at the vertical end walls of the melt layer. The temperature at the vertical wall is uniform along its height with a stability of $\pm 0.1°C$. Figure 1 is a schematic of the Ga–5In specimen. The dimensions of the test volume is $50 \times 35 \times 2$ mm ($L \times H \times d$). An overflow volume is provided for volume expression.

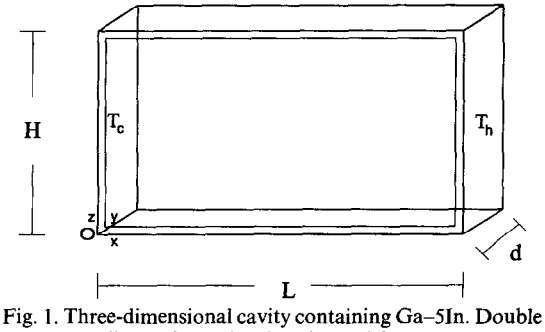

Fig. 1. Three-dimensional cavity containing Ga–5In. Double line in front sketches the lead frame.

The Grashof number is defined to characterize the fluid flow in the natural convection case as follows:

$$Gr = \frac{g\beta \frac{\Delta T}{1} H^4}{\nu^2}. \quad (1)$$

Since thermophysical data are not available for Ga–In solutions, we calculated the properties by interpolating the properties of pure Ga and pure In based on the mole fractions of each component being present, assuming ideal solution behavior (Table 1). The data sources we used for Table 1 do not include information on error estimates of the properties of the pure elements. For the pure elements the error is considered negligible for most purposes. Thus an error evaluation of the calculated properties for the alloy under investigation is limited to the weighing error during the preparation of the master alloy. In the case of the postulated conductive state, the characteristic length in the Gr is measured at the bottom of the liquid layer (designated as Gr_l). Clearly this length

Table 1. Properties of gallium, indium and Ga–5In

Parameter	Symbol	Value	Units	Refs.
	Gallium			
Melting point	T_m	29.78	°C	[35]
Volumetric coefficient of thermal expansion (373 K)	β	1.2×10^{-4}	K^{-1}	[35]
Viscosity	μ	2.04×10^{-3}	kg m^{-1} s^{-1}	[36]
Density	ρ^m (302.78 K)	6094.70	kg m^{-3}	[35]
m = melt; s = solid	ρ^s (302.65 K)	5903.70		[35]
Momentum diffusivity	ν	3.347×10^{-7}	m^2 s^{-1}	$\nu = (\mu/\rho)$
Thermal conductivity	k^m (350 K)	28.68	W m^{-1} K^{-1}	[35]
m = melt; s = solid	k^s (302.78 K)	33.49		[35]
Specific heat (500 K)	c_p	384.7	J kg^{-1} K^{-1}	[35]
Thermal diffusivity	κ^m	1.223×10^{-5}	m^2 s^{-1}	$\kappa = (k^m/\rho c_p)$
Mass absorption coefficient (at $K_{\alpha,W} = 60$ keV)	$(\mu/\rho)_{0,Ga}$	12.97	m^2 kg^{-1}	[37]
Self-diffusion coefficient	D_{Ga}	1.61×10^{-9}	m^2 s^{-1}	[38]
	Indium			
Melting point	T_m	156.63	°C	[32]
Volumetric coefficient of thermal expansion (293 K)	β	0.97×10^{-4}	K^{-1}	[36]
Viscosity	μ	1.69×10^{-3}	kg m^{-1} s^{-1}	[36]
Density	ρ^m (429.4 K)	7030	kg m^{-3}	[36]
m = melt; s = solid	ρ^s (293 K)	7300		[36]
	ρ^m (303 K)	7113		calc.
Momentum diffusivity	ν	2.404×10^{-7}	m^2 s^{-1}	$\nu = (\mu/\rho)$
Thermal conductivity	k^m (429.4 K)	41.87	W m^{-1} K^{-1}	[36]
m = melt; s = solid	k^s (273 K)	83.7		[32]
Specific heat (429.63 K)	c_p	257	J kg^{-1} k^{-1}	[32]
Thermal diffusivity	κ^m	2.318×10^{-5}	m^2 s^{-1}	$\kappa^m = (k^m/\rho c_p)$
Mass absorption coefficient (at $K_{\alpha,W} = 60$ keV)	$(\mu/\rho)_{0,In}$	46.83	m^2 kg^{-1}	[37]
Self-diffusion coefficient	D_{In}	1.80×10^{-9}	m^2 s^{-1}	[38]
	Ga–5 w% In (Ga–3.1 atomic % In)			
Melting point	T_m	25	°C	[32]
Density (m = melt)	ρ^m	6123.7	kg m^{-3}	calc.
Volumetric coefficient of thermal expansion (293 K)	β	1.19×10^{-4}	K^{-1}	calc.
Momentum diffusivity	ν	3.318×10^{-7}	m^2 s^{-1}	calc.
Thermal conductivity	k^m	29.09	W m^{-1} K^{-1}	calc.
Mass absorption	μ/ρ	13.99	m^2 kg^{-1}	calc.
Diffusion coefficient	D_{Ga-In}	1.525×10^{-9}	m^2 s^{-1}	calc. [38]

definition is ambiguous; the choice is based on the slope of the interface during melting. In the fully convective state, the length is measured at the top of the cavity and designated as Gr_u.

It should be noted that the visualized area is slightly smaller (~2% on all sides) than the cavity due to the required lead framing of the test volume [29]. The lead masking frame is sketched in Fig. 1 as a double line. Image processing included re-sizing the images, false coloring and gray shade adjustments to improve contrast and ease visualization.

3. EXPERIMENTS AND RESULTS

Pure gallium (6N purity) was added into the test cell and isothermalized for 24 h at 40°C. Using constant CCD camera and brightness/contrast settings on the image processor, a radiation intensity distribution after absorption by the isothermal liquid gallium is obtained and kept as background image. Pellets of Indium (6N purity) were then added into the cavity containing gallium such that the final composition of the alloy was Ga–5In. Indium has a higher density than gallium and therefore also a higher X-ray absorption (Table 1). Therefore, X-ray radioscopy will reveal darker regions wherever there is more indium in the gallium melt.

Figure 2(a) shows pellets of indium as dark spots in the upper central portion of the cavity. These indium pellets dissolve and diffuse into the gallium melt. However, since indium is heavier than gallium it appears to settle to the bottom of the test cell. At the right side in Fig. 2(a), a vertical trail of dark dissolving indium flowing to the bottom is visualized. The darker region at the bottom of the test cell [Fig. 2(b)] visualizes the sedimented indium. This settling rate is much faster than the diffusion rate of indium in gallium. The diffusion coefficient for the Ga–5In system was calculated after [38] to be approximately 1.525×10^{-9} m^2 s^{-1}.

Figure 2(c) is a processed gray-scale image of the isothermal Ga–5In alloy at 40°C about 24 h after addition of the indium. For improved visualization purposes the vertical linear gray level profile is processed into a step-function of averaged density values.

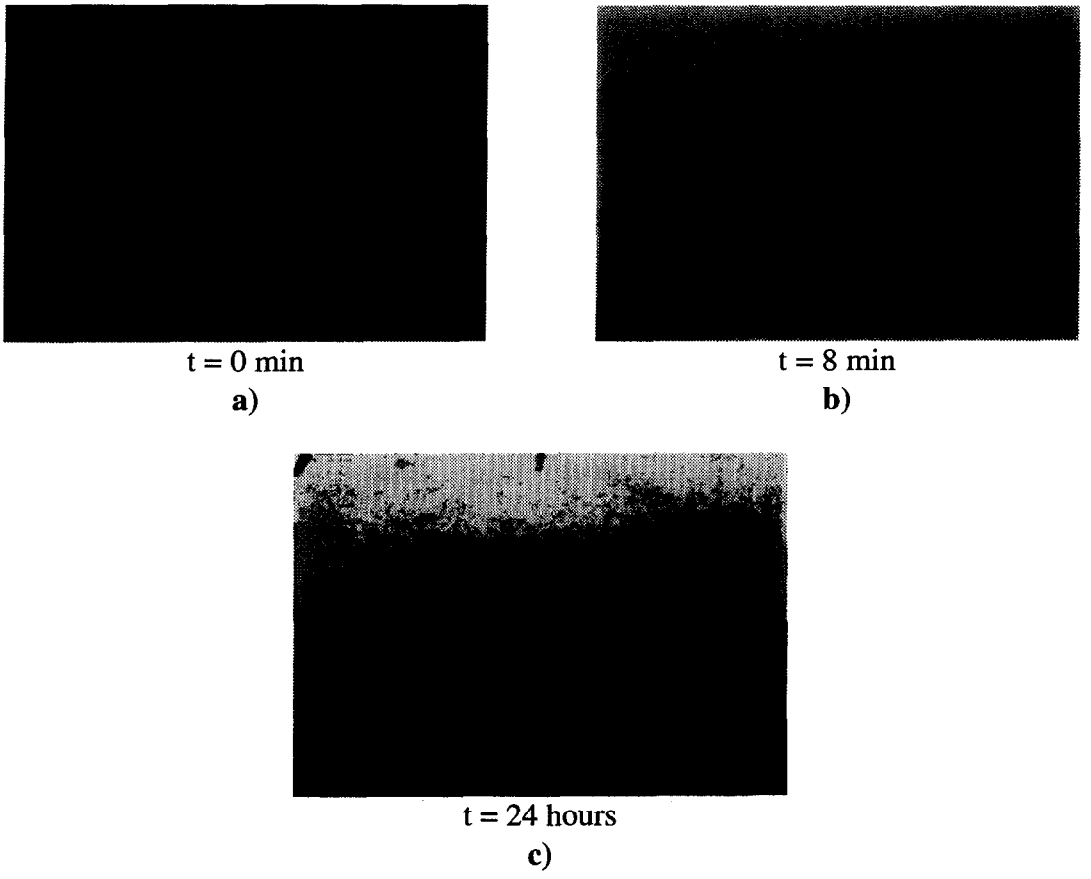

Fig. 2. Dissolution of indium pellets upon addition to a gallium melt at 40°C. Gravitational segregation in the Ga–5In alloy. (a), (b) Images not processed, (c) image processed.

This way the visualization emulates fringe patterns similar to those known from optical interferometry. Fringes thus should not be interpreted as stratified liquid layers! As in interferometry, equal fringe widths represent a linear property profile (i.e. concentration) orthogonal to the fringes; non-equal fringe widths represent a nonlinear profile.

This Ga–5In melt, with a clearly defined vertical concentration stratification was convectively mixed by setting up a large temperature difference (30°C) between the hot and cold sides of the cavity [Figs. 3(a)–(c)]. These images clearly show the development of thermosolutal convection in the melt. Plumes can be seen rising along the right, hot wall of the test cell and flowing toward the cold side. Apparently vertically layered roll cells do not develop.

After 10 h of convective mixing the temperature on both sides of the cavity was set to 40°C to isothermalize the melt for about 3 h. Even with such a short isothermalization time, visualization of the isothermal melt in Fig. 3(d) revealed weak segregation.

To avoid further vertical concentration segregation, the Ga–5In melt was solidified right away, with the goal to obtain a homogeneous solid alloy. Rapid cooling of the melt was done by ramping the constant temperature baths at a fast rate (~ 50 K h^{-1}). Figure 4 includes images of two Ga–5In solids from two separate solidification experiments. Dark regions are indium-rich, light areas are indium-depleted or gallium-rich. Dendrites are visualized in Fig. 4(b). It can be seen that with each experiment the structure of the solid and chemical element distribution may be quite different.

The solid alloy is first isothermalized at 0°C for about 2 h. Subsequently a natural convection experiment is started by quasi-steady application of a horizontal temperature gradient. For this purpose the hot side was first ramped in two hours to $T_h = 25$°C at the alloy/thermode interface, leaving the cold temperature set at 0°C. The temperature gradient in the solid being $\Delta T/L = 5.2$ K cm^{-1}. To start the melting process, the hot side temperature was increased at a rate of less than 0.01 K min^{-1} and halted at specific plateaus. Occasionally the cold side temperature was also slowly increased.

Figures 5(a)–(f) show a series of processed images taken with increasing temperature difference across the liquid layer. The liquid phase is color-coded, the solid is in gray shades. For comparison the sensitivity

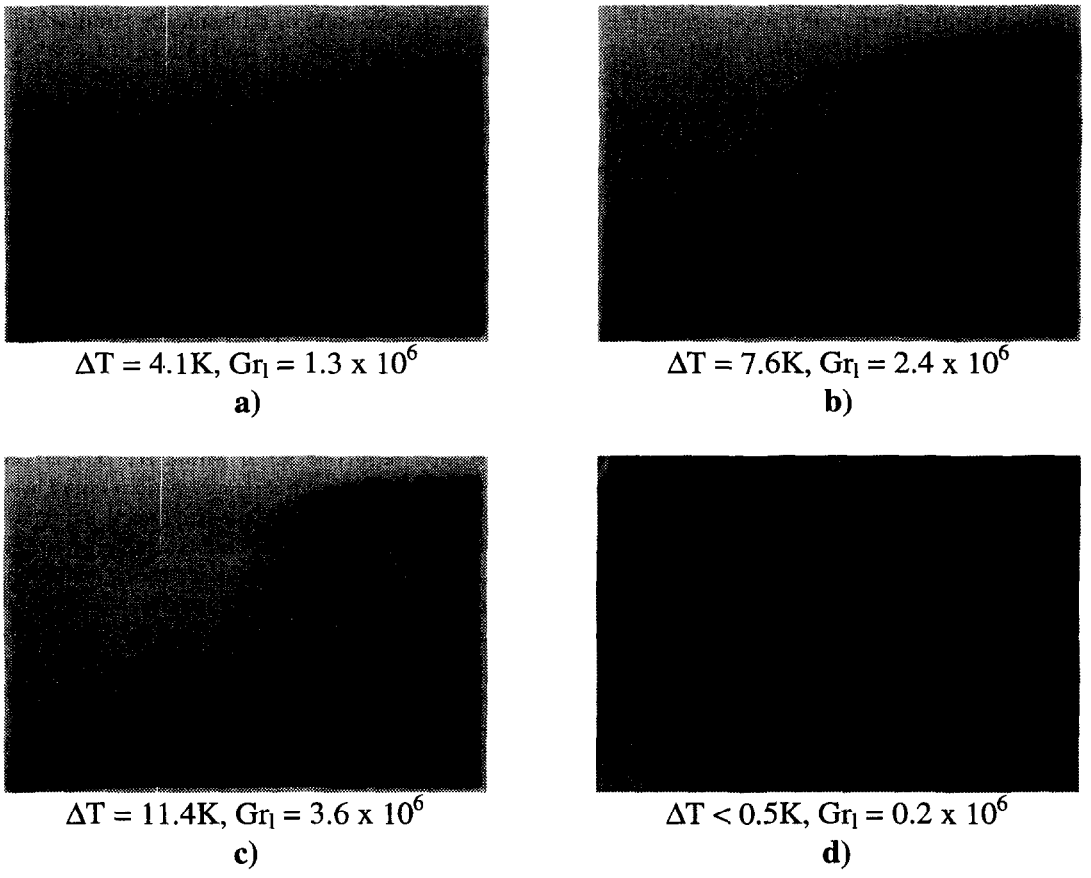

Fig. 3. (a)–(c) Time dependent thermosolutal convection in the Ga–5In alloy melt subjected to a temperature gradient, (d) isothermal Ga–5In at 40°C.

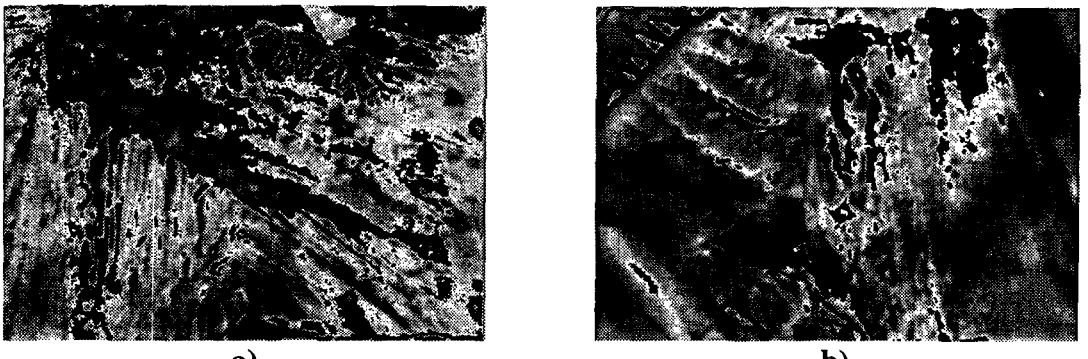

Fig. 4. Ga–5In solid obtained from two different experiments upon rapid cooling and solidification of the undercooled melt.

of the radiation intensity measurements is kept constant in all pictures. Each fringe is assigned a specific color. The chosen colors are in order of increasing indium concentration: red, yellow, magenta, green, cyan, blue. The ramping, now at a rate of 4 K hr^{-1}, is halted at every 0.5 K change and the system is allowed to thermally equilibrate in order to achieve quasi-steady heating conditions.

The solid melts while forming a sloped interface shape, although each thermode provides a constant vertical temperature distribution (±0.05°C) at the wall/alloy interface, leading to a vertically homogeneous temperature in the melt. At the upper boundary the liquid does extend horizontally much less into the test cell than along the bottom of the layer. This interface shape is different from a morphology

imposed by convective flow in a single element metallic melt [6–8]. Density visualization in the melt reveals a vertical chemical stratification. The lower layers of the stratified melt contain more of the heavier indium than the layer immediately above it (compare Fig. 2). Hence we postulate that the heat transfer in the stratified melt is primarily by conduction, and advection, if any, is weak. Note that the current measurement technique does not provide flow velocity measurements which could possibly quantify any advection.

With further increase of ΔT in the liquid [$Gr_l = 1.7 \times 10^6$, Fig. 5(b)], the solid–liquid interface starts to deform from the bottom upward. This morphology change is correlated to thermosolutal convection in the lower portion of the melt. The convecting melt provides uniform species mixing which is visualized by the area of uniform radiation coded in blue. Above this layer the liquid remains in a conductive, vertically stratified state and the interface remains slanted. The transition from a conductive state to a convective state begins at about $Gr_l = 1.7 \times 10^6$. This convection roll cell beneath the conductive liquid layer is an equilibrium pattern and does not change with time unless the Grashof number is changed.

As the solid–liquid interface is a moving boundary, the onset is dependent on the location of the interface, which is determined by the temperatures applied at the end walls. The threshold then is not a fixed critical value as in Rayleigh–Bénard convection with fixed boundaries. With increasing Grashof number, the convecting sub-layer grows larger and the free moving interface adjusts constantly to the convective flow and the actual temperature of the thermodes. The convecting liquid finds an equilibrium volume with a clear impact on the solid–liquid interface morphology [Fig. 5(c)]. The blue-colored convecting layer has almost a square shape and the color reflects that the melt is indium-rich and concentrationally well mixed. The horizontal fringes show also that the concentration of indium in the melt above the convecting layer still decreases as a function of height. That liquid remains chemically stratified and the interface remains sloped. The upper melt stratification, and the interface morphology require that heat transport in that layer remains conductive.

At this point of this experiment, the temperature at the cold side is also increased quasi-steadily. This leads to more melting of the solid and an increased melt length l along the bottom of the layer; which means that the Grashof number [equation (1)] is reduced (although the temperature difference increases slightly because of the continued increase in temperature at the hot wall). It can be seen from Figs. 5(d)–(f) that the blue coloring recedes to a horizontal layer at the bottom which means that the indium sediments again toward the bottom. This means also that the convective flow comes to a halt as the Grashof number drops below $Gr_l \approx 2.8 \times 10^6$, and the melt transitions back to a conductive state of a chemically stratified melt. The solid–liquid interface angle adjusts to about 45°.

Continuing with the equilibrium pattern of Fig. 5(f), the Grashof number is increased now by cooling the cold side quasi-steadily. More solid freezes [Fig. 6(a)] and is visualized as a lighter solid band along the interface. The light color of the new solid indicates that less radiation absorbing α-gallium is solidifying. Although the temperature gradient is about constant, the Grashof number is increased due to the reduced length l. The color-coding is also in order of increasing indium concentration: red, yellow, magenta, green, cyan, blue.

The interface starts to deform in the lower region at about $Gr_l = 2.4 \times 10^6$ [Fig. 6(b)] as thermosolutal convection begins to set-in within the bottom sublayer. The convecting blue (indium-rich) liquid leaves a clear mark at the interface [Fig. 6(c)]. Above the convective layer the fluid remains vertically stratified and in a conductive state as shown by the color-coded horizontal fringes. The convecting thermosolutal region is well mixed and of almost uniform cyan color, i.e. uniform species concentration. The change in color from blue to cyan, which corresponds to a specific value of the gray-scale step-function, means that as more liquid gets mixed with superposed liquid of lesser indium concentration, the average indium concentration of the convecting liquid is reduced to a value below the intensity setting for the blue color. Figure 6(d) still has a small upper stratified layer in a conductive state which eventually disappears completely [Fig. 6(e)] at about $Gr_u = 4.2 \times 10^6$. In this case the convective flow is fully developed and the dominant heat transfer mechanism in the melt is by convection. As the radiation transmission through the melt increases, the color of the fringe switches to green indicating a further reduction in indium concentration as all of the upper indium-depleted melt has become mixed with the rest of the melt. The green fringe is also visualized at mid-height of the stratified melt in Figs. 6(a), (b) and thus represents the original Ga–5In composition.

4. DISCUSSION OF RESULTS

The Grashof number range for the transition from a conductive to a fully convective state goes in this case from $2.4 < Gr \times 10^{-6} < 4.2$. Below $Gr_l = 2.4 \times 10^6$ the melt is chemically stratified and the solid–liquid interface is at an angle to the vertical line. Above $Gr_u = 4.2 \times 10^6$ all the melt is uniformly mixed and convecting. A natural convection situation as in Fig. 6(e) has been modeled by Shyy and Chen [3] using uniform thermophysical properties. In between $Gr_l = 2.4 \times 10^6$ and $Gr_u = 4.2 \times 10^6$, the lower portion of the melt is in a convecting state, whereas the upper liquid is chemically stratified and in a conductive state.

For the analysis we convert the intensity field to density and apply principles from optical interferometry. Based on the single color (green) fringe we

$\Delta T = 1.4$ K, $Gr_l = 1.0 \times 10^6$

a)

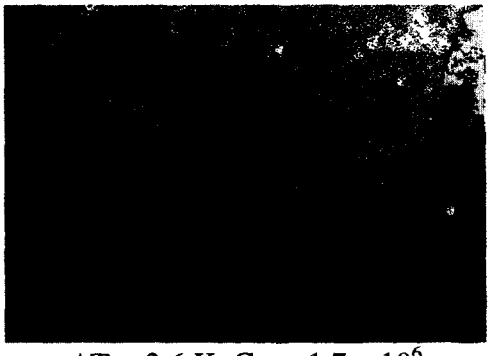

$\Delta T = 2.6$ K, $Gr_l = 1.7 \times 10^6$

b)

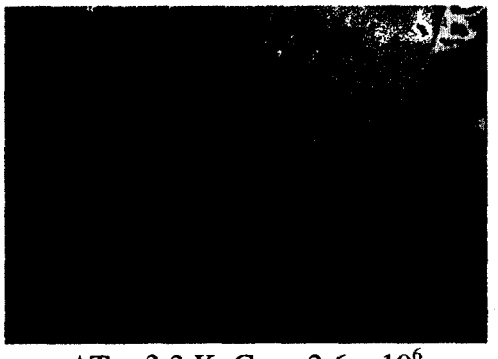

$\Delta T = 3.3$ K, $Gr_l = 2.6 \times 10^6$

c)

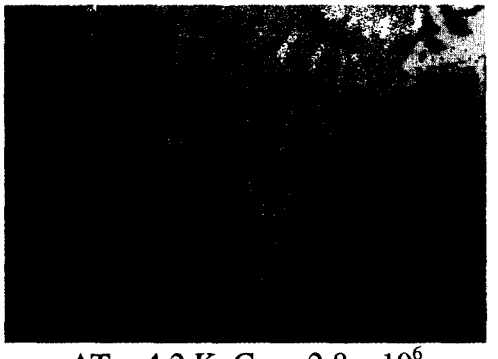

$\Delta T = 4.2$ K, $Gr_l = 2.8 \times 10^6$

d)

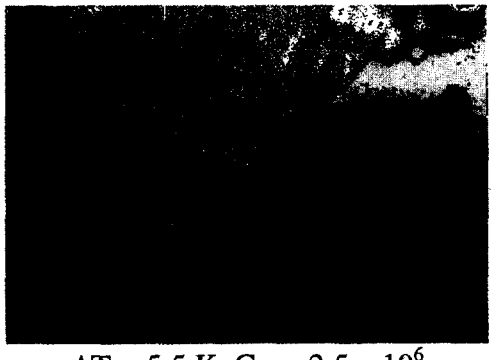

$\Delta T = 5.5$ K, $Gr_l = 2.5 \times 10^6$

e)

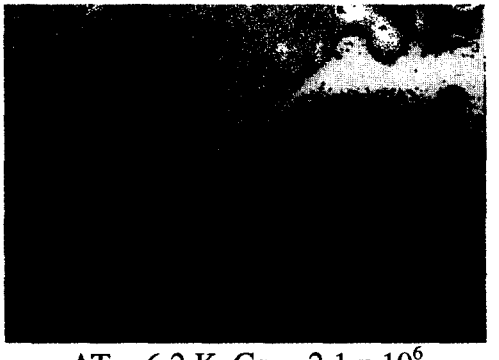

$\Delta T = 6.2$ K, $Gr_l = 2.1 \times 10^6$

f)

Fig. 5. Increase and decrease of the temperature gradient resulting in the transition from conductive to partially convective and back to conductive state.

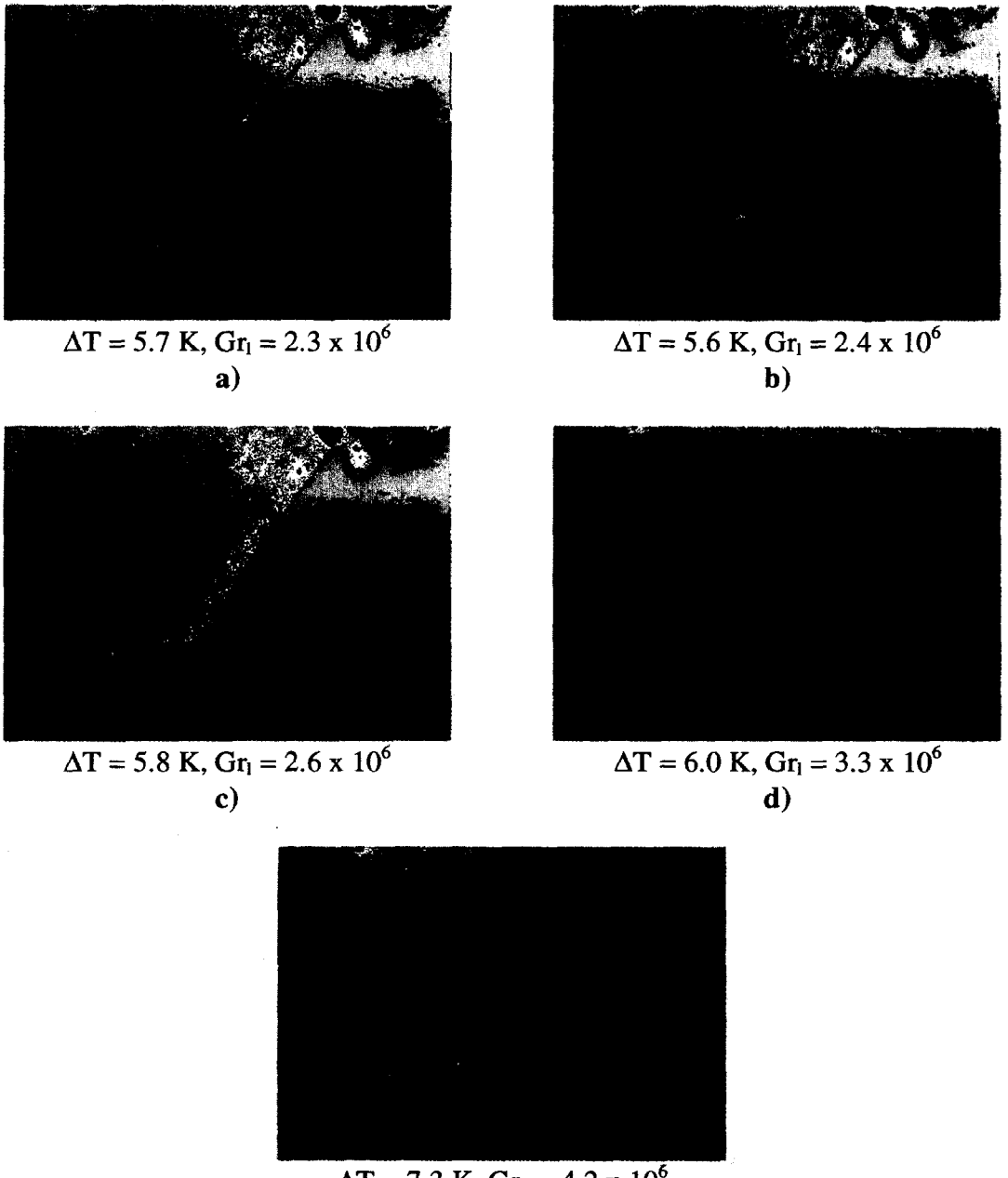

$\Delta T = 5.7$ K, $Gr_l = 2.3 \times 10^6$
a)

$\Delta T = 5.6$ K, $Gr_l = 2.4 \times 10^6$
b)

$\Delta T = 5.8$ K, $Gr_l = 2.6 \times 10^6$
c)

$\Delta T = 6.0$ K, $Gr_l = 3.3 \times 10^6$
d)

$\Delta T = 7.3$ K, $Gr_u = 4.2 \times 10^6$
e)

Fig. 6. Transition from the conductive to the fully convective thermosolutal state.

assume that in Fig. 6(e) the convecting melt is well mixed and chemically uniform within resolution settings. We assume that the visualized fringe is due to a density change as a function of temperature only and postulate that the density change spans one full fringe width. Local temperature measurements are available from thermocouples at the interface and at the hot side wall. This model gives the density change $\rho(T)$ across the liquid layer, visualized as one fringe. We calculate $(\Delta\rho/\text{color}) = 5.3 \pm 0.5\ \text{kg m}^{-3}$, including the error inherent in the fringe-width determination and the weighing. In the cases where we postulate a conductive state, Figs. 2(c), 5(e), (f), 6(a), the increased number of fringes, at smaller temperature difference than Fig. 6(e), must therefore originate from radiation absorption of the indium distribution. The change in measured radiation intensity can thus be correlated to concentration stratification (Appendix).

The calculations for the concentrational stratification give in case of Fig. 2(c) a value of $\Delta C = 0.14$ w% indium, or 0.04 w% cm^{-1}. In the Figs. 5(e), (f) and 6(a), the stratification is larger with $\Delta C = 0.18$ w% indium or 0.05 w% cm^{-1}. The difference between both situations is that one case describes a cavity entirely filled with a melt, and in the other case we have a cavity partially filled with a structured solid that melts. We did also observe that the gravitational segregation develops as the function of time.

The observed segregation is much higher than the calculated segregation obtained from current models, which is about $\Delta C = 3 \times 10^{-7}$ using mass fractions, or 3×10^{-5} w% indium [33, 34]. Note that our measuring technique would not resolve such a small segregation! For Fig. 2(c), the composition of the liquid alloy is estimated at the top at Ga–4.93In and at the bottom at Ga–5.07In. With the error in indium weighing of $< \pm 0.005$ w% and the error in fringe-width determination, these values are accurate to better than ± 0.02 w%. Similarly, for Figs. 5(e), (f) and 6(a), the melt composition at the top of the liquid layer is Ga–4.91In and at the bottom the composition is Ga–5.09In. In Figs. 5 and 6 we also find the green fringe at mid-height, which justifies our assumption that the original composition Ga–5In is found at mid-height of the liquid layer. Based on the five fringes in the Figs. 5 and 6 the density difference between top and bottom is $\Delta\rho_{\text{tb}} = 10.7 \pm 0.5\ \text{kg m}^{-3}$. Such a density stratification is small, but could provide sufficient stabilization of the liquid layer against thermal (infinitesimal) perturbations.

Thermosolutal calculations need relevant dimensionless parameters, including the thermosolutal parameter $S = \beta_S \Delta C / \beta_T \Delta T$ [33]. Above we provided an estimate of the concentration stratification $\Delta C = 0.0018$ at the horizontal temperature difference $\Delta T = 5.7$ K [Fig. 6(a)], just before onset of convection. The thermal expansion coefficient of the Ga–5In can be calculated on the molar fraction basis as $\beta_T = 1.19 \times 10^{-4}\ \text{C}^{-1}$. The expansion coefficient for the chemical species can be estimated as $\beta_S = 0.14$. Thus the parameter $S = \approx 0.37$.

If the solid is different in microstructure (Fig. 4) the melting and morphology of the interface as well as the amount of chemical stratification are slightly different; but the conductive–convective threshold is repeatable [33]. Especially the interface morphology varies between experiments started from different solid structures. Higher vertical chemical stratification raises the critical temperature (critical Gr) for the transition.

Upon melting, we observe a sloped interface shape which needs explanation. As the first solid melts quasi-steadily at the vertical end wall, gravitational segregation occurs as the heavier indium settles to the bottom. The thermal conductivity ratio of liquid gallium to liquid indium is 0.69. With the evaluated chemical stratification for Fig. 6(a), we calculate the thermal conductivity of the alloy (using molar fractions) along the top of the layer as $k = 29.084\ \text{W m}^{-1}\ \text{K}^{-1}$ and along the bottom as $k = 29.095\ \text{W m}^{-1}\ \text{K}^{-1}$, or a vertical change of $\Delta k = 0.011\ \text{W m}^{-1}\ \text{K}^{-1}$, or a thermal conductivity gradient of $\partial k/\partial H = 0.3\ \text{W m}^{-2}\ \text{K}^{-1}$. This gradient is small, however the slope of the interface may indicate a strong impact of melt conductivity on the system. The calculations of the thermal conductivity data are purely mathematical. They are not measurements and are included to assess possible mechanisms for the observed conductive–convective threshold in metallic alloy melts.

A second potential reason for the sloped interface shape is gathered for the phase diagram of the alloy. It shows that the solidus of hypo-eutectic Ga–In is very steep. The measured concentration difference between top and bottom of $\Delta C = 0.18$ w% indium would vary the interface temperature from top to bottom by much less than 1°C. The estimated temperature at the interface of constant $T = 25$°C thus is a crude, but valid assumption. The shallower liquidus slope could account for a $\Delta C = 0.18$ w% within temperature in homogeneities of the test cell. As diffusion in the melt is sufficiently high to reach equilibrium within reasonable time, we would expect chemical uniformity of the melt as a function of time. However, the opposite behavior is observed: the chemical segregation increases as a function of time when Gr = constant.

Another parameter which would need scrutiny is the viscosity and its dependence on concentration. Eventually it needs to be evaluated whether the melt is, or is not, a perfectly homogeneous single phase liquid. Which plausible cause is the dominating one leading to the observations reported here, cannot be decided from the present experiments. Therefore, we can only postulate that the slope of the solid–liquid interface is defined by the combined effects of non-Boussinesq properties of the melt and by the thermodynamics and kinetics at the interface.

In one sequence of two experiments we observe two different Grashof numbers for the onset of convection

(Figs. 5 and 6). A plausible explanation of that observation lies within the composition of the melt. In the first experiment the cold side temperature was reduced to solidify more alloy. The visualization showed that the new solid is more transparent, thus must be of α-Ga composition. This requires that during solidification, indium was rejected into the melt and now the melt concentration is increased and the concentration profile is changed. In support of that argument we did observe higher threshold *Gr* in eutectic Ga–In melts [20].

One last visualization needs discussion: in the Ga–5In alloy, when the horizontal temperature gradient is increased, thermosolutal convective flow develops in a lower sub-layer of finite vertical extension. That convective flow creates a dent in the solid–liquid interface. The convecting liquid becomes uniformly mixed, visualized as a constant radiation intensity (uniform color). Above the convecting layer the liquid remains vertically stratified and in a conductive state. That state is in equilibrium at constant *Gr*. If vertically staggered roll cells would develop in the steady-state melt at small *Gr*, each roll cell would markedly indent the interface. No such indentations are observed. Thus the experimental evidence indicates a conductive state at low *Gr*.

At this point we want to address the confidence in the calculation of the thermophysical property data and Grashof numbers. All properties for the alloy were calculated from properties of the pure elements. The sources for these data [32, 35] do not give any error margins for the data, considering them well established as defined from many measurements. So, our error assessment is limited to the preparation of the master alloy and the resolution limit of the experimental technique. The master alloy can be fabricated with high precision using electronic scales (resolution: 0.1 mg), we estimated an error of less than 0.005 w% In. The largest error comes from the radiation intensity visualization and thus the fringe demarcation. Here we estimate that we do have a potential error of 10% in the definition of the span of one fringe, a level of accuracy commonly achieved in interferometry. Thus we conclude that the visualized density data are accurate to at least 10%. Another error is in the calculation of the Grashof numbers. As we can only estimate the temperature of the solid–melt interface by 10% accuracy, the Grashof number is also accurate to 10% at best. Considering possible errors in the property data, the accuracy of *Gr* may be only about 20% in the worst case scenario.

5. CONCLUSION

Under quasi-steady conditions, the dissolved indium did gravitationally segregate to the bottom of the liquid gallium layer. The concentration gradient between top and bottom of the melt is calculated from image processing to be about 0.063 w% cm^{-1} indium. In an isothermal melt, the gravitational segregation develops as a function of time. When a horizontal temperature gradient is applied to the melting alloy specimen, a conductive–convective threshold for the onset of natural convection is observed. This threshold may be explained by the stabilizing vertical concentration gradient.

During the conduction–convection transition, thermosolutal convection starts in the lower indium-rich sub-layer of the melt, and not in all the melt. Above this convecting layer the extra liquid remains in a conductive and concentrationally stratified state. As the solid–liquid interface is a moving boundary, the sub-layer convective state finds an equilibrium pattern at constant Grashof number. The transition from a conductive melt to a fully convective flow in the Ga–5In melt extended from $1.7 < Gr \times 10^{-6} < 4.2$. The transition range is dependent on the average concentration in the melt, which depends also on the macrosegregation in the starting solid specimen. Such a conductive–convective transition range has not been predicted by analytical or numerical models, nor has a thermosolutal roll cell developing in a sublayer of the meltphase been predicted.

Acknowledgements—Support by National Science Foundation (NSF) under grants CTS-8906846 and CTS-9114775, National Aeronautics and Space Administration (NASA) under NCC3-210, and ALCOA Foundation is greatly appreciated.

REFERENCES

1. Turner, J. S., *Buoyancy Effects in Fluids*. Cambridge University Press, Cambridge, U.K., 1973.
2. Kaddeche, S., Ben-Hadid, H. and Henry, D., Macrosegregation and convection in the horizontal Bridgman configuration. *Journal of Crystal Growth*, 1994, **135**, 341–353.
3. Shyy, W. and Chen, M.-H., Effect of Prandtl number of buoyancy-induced transport processes with and without solidification. *International Journal of Heat and Mass Transfer*, 1990, **33**, 2565–2578.
4. Ostrach, S., Fluid mechanics in crystal growth. *Journal of Fluids Engineering*, 1983, **105**, 5–20.
5. Viskanta, R., Heat transfer during-melting and solidification of metals. *Journal of Heat Transfer*, 1988, **110**, 1205–1219.
6. Gau, C. and Viskanta, R., Melting and solidification of a pure metal on a vertical wall. *Journal of Heat Transfer*, 1986, **108**, 174–181.
7. Viswanath, R. and Jaluria, Y., Numerical simulation of phase change problems in enclosures: a comparison of different approaches. *In Heat Transfer in Phase Change*, ASME-HTD-205, 1992, pp. 55–62.
8. Campbell, T. A. and Koster, J. N., Visualization of liquid/solid interface morphologies in gallium subject to natural convection. *Journal of Crystal Growth*, 1994, **140**, 414–425.
9. Hurle, D. T., Jakeman, E. and Johnson, C. P., Convective temperature oscillations in molten gallium. *Journal of Fluid Mechanics*, 1974, **64**, 565–576.
10. Hart, J., Stability of thin non-rotating Hadley circulations. *J. Atm. Sci.*, 1972, **29**, 687–697.
11. Camel, D., Tison, P. and Favier, J. J., Marangoni flow regimes in liquid metals. *Acta Astronautica*, 1986, **13**, 723–726.
12. Stewart, M. J. and Weinberg, F., Flow of liquid tin in a

square enclosure. *Transactions of AIME*, 1969, **245,** 2108–2110.
13. Semiatin, S. I. and McQuay, P. A., Segregation and homogenization of near-gamma titanium aluminide. *Metallurgical Transactions A*, 1992, **23A,** 149–161.
14. Hulme, K. F. and Mullin, J. B., Indium–antimonide—a review of its preparation, properties and device applications. *Solid-State Electronics*, 1962, **5,** 211–247.
15. Mullin, J. B., Segregation in InSb. In *Compound Semiconductor VI, Preparation of III–V Compounds*, ed. R. K. Willardson and M. L. Goeling. Reinhold Publishing, New York, 1962, pp. 365–381.
16. Watson, J. H., Liquation or 'inverse segregation' in the silver–copper alloys. *J. Inst. Metals*, 1932, **49,** 347–362.
17. Allen, B. C. and Isserow, S., Segregation at the eutectic temperature. *Acta Metallurgica*, 1957, **5,** 465–472.
18. Reijonen, H. and Forstén, J., Observation of segregation in Sn–Cd alloy melts using neutron radiography. *Journal of Crystal Growth*, 1972, **12,** 61–62.
19. Galzov, V. M., Pavlova, L. M. and Stankus, S. V., Liquation phenomena in CMT melts and their volumetric properties. In *Centrifugal Materials Processing*, 3rd edn, ed. L. L. Regel and W. R. Wilcox. Plenum, New York, 1997.
20. Koster, J. N., Derebail, R. and Grötzbach, A., Visualization of convective solidification in a vertical layer of eutectic Ga–In melt. *Applied Physics A*, 1997, **64,** 45–54.
21. Glicksman, M. E. and Sokolowski, R. S., Gravitational influence on binary alloy melt equilibria. *Advances in Space Research*, 1983, **3,** 129–134.
22. Kürten, M. and Schilz, J., Czochralski growth of Si_xGe_{1-x} single crystals. *Journal of Crystal Growth*, 1994, **139,** 1–5.
23. Schilz, J. and Romanenko, V. N., Review: bulk growth of silicon–germanium solid solutions. *J. Mat. Sci: Materials in Electronics*, 1995, **6,** 265–279.
24. Barber, P. G., Crouch, R. K., Fripp, A. L., Debnam, W. J., Berry, R. F. and Simchick, R., A procedure to visualise the melt–solid interface in Bridgman grown germanium. *Journal of Crystal Growth*, 1986, **74,** 228–230.
25. Kakimoto, K., Eguchi, M., Watanabe, H. and Hibiya, T., *In situ* observation of solid–liquid interface shape by X-ray radiography during silicon single crystal growth. *Journal of Crystal Growth*, 1990, **99,** 665–669.
26. Kaukler, W. F. and Rosenberger, F., X-ray microscopic observations of metal solidification dynamics. *Metal. Mat. Trans. A*, 1994, **25A,** 1775–1777.
27. MacGillavry, C. H. and Rieck, G. D., *International Tables for X-ray Crystallography*, Vol. III. The Kynoch Press, Birmingham, U.K., 1962.
28. Pool, R. E. and Koster, J. N., Visualization of density fields in liquid metals. *International Journal of Heat and Mass Transfer*, 1994, **37,** 2583–2587.
29. Koster, J. N., Seidel, T. and Derebail, R., A radioscopic technique to study convective fluid dynamics in opaque liquid metals. *Journal of Fluid Mechanics*, 1997, **343,** 29–41.
30. Campbell, T. A. and Koster, J. N., Radioscopic visualization of indium antimonide growth by vertical Bridgman–Stockbarger technique. *Journal of Crystal Growth*, 1995, **147,** 408–410.
31. Campbell, T. A. and Koster, J. N., A novel vertical Bridgman–Stockbarger crystal growth system with visualization capability. *Meas. Sci. Technol.*, 1995, **6,** 472–476.
32. White, C. E. T. and Okamoto, H., Phase diagrams of indium alloys and their engineering applications. *Monograph Series on Alloy Phase Diagrams*, 1st edn. ASM International, Materials Park, OH, p. 2.
33. Koster, J. N. and Derebail, R., A threshold for natural convection in binary metallic alloys. *Heat and Mass Transfer*, 1997, **32,** 489–498.
34. DeHoff, R. T., *Thermodynamics in Materials Science*. McGraw-Hill, New York, 1993.
35. Murray, G. T. and Lograsso, T. A., *Metals Handbook, Vol. 2—Properties and Selection: Nonferrous Alloys and Special-Purpose Materials*, 10th edn. ASM International, Materials Park, OH, 1990, pp. 1114–1115.
36. Carter, G. F., *Metals Handbook—Desk Edition*, ed. H. E. Boyer and T. L. Gall. 1st edn. American Society for Metals, Metals Park, OH, pp. 2–19.
37. Burr, A. F., *CRC Handbook of Chemistry and Physics*, ed. R. C. Weast and D. R. Lide, 70th edn. CRC Press Inc., Boca Raton, FL, pp. E149 E151.
38. Savinstev, P. A., Akhkubekov, A. A., Getazheev, K. A., Rogov, V. I. and Savvin, V. S., Determination of diffusion and activity coefficients in the gallium–indium system by the contact–melting method. *Soviet Physics Journal*, 1971, **4,** 467–470.

APPENDIX

Calculation of $\Delta\rho_{In}$ for the chemically stratified case

First we need the radiation intensity calculations for Fig. 6(e). Radiation intensity varies as [33]:

$$\frac{\Delta I_1}{I_0 d} = \left(\frac{\mu}{\rho}\right)_{Ga\text{–}In} \Delta\rho_{Ga\text{–}In}. \tag{A1}$$

Assuming that for this case, the indium is uniformly mixed with the gallium and that its mass fraction is 5 w% or 3.1 atomic percent in the alloy, $(\mu/\rho)_{Ga\text{–}In}$ is a material constant of the alloy which we can calculate with atomic fractions X of the elements [33]:

$$\left(\frac{\mu}{\rho}\right)_{Ga\text{–}In} = 4.683*0.03 + 1.297*0.97 = 1.399 \text{ cm}^2 \text{ g}^{-1}.$$

With $\Delta\rho_{Ga\text{–}In} = 5.3 \times 10^{-3}$ g cm^{-3} and with equation (A1), we get

$$\Delta I_1/(I_0 d) = 0.0074 \text{ cm}^{-1}.$$

Next we calculate the radiation intensity in the case of the chemically stratified melt, Figs. 2(c), 5, and 6. We assume a model of Ga and In sheets. Then we suppose that ΔI_2 is due only to the chemical segregation of indium and get:

$$\Delta I_2 = \Delta I_{Ga} + \Delta I_{In} \tag{A2}$$

as the change of intensity is caused by a higher indium concentration at the bottom than at the top of the melt layer. Let us consider two small quantities of alloy of the same volume. The first one models the alloy at the top of the melt, the second models the alloy at the bottom of the melt layer [33].

Then

$$\frac{m_{Ga1}}{V_{Ga1}} = \frac{m_{Ga2}}{V_{Ga2}} = \rho_{Ga} \quad \text{(density of pure gallium)}$$

$$\frac{m_{Ga1}}{V} = \rho_{Ga1} \quad \text{(density of gallium in case 1)}.$$

In case no. 2, the density of indium has increased. In V there is more indium, the new mass of indium is: $m_{In2} = m_{In1} + dm_{In}$, where dm_{In} occupies a small volume v.

Then

$$V_{Ga2} = V_{Ga1} - v = V_{Ga1} - \frac{dm_{In}}{\rho_{In}}.$$

Within V_{Ga2} there is

$$m_{Ga2} = \rho_{Ga}\left(V_{Ga1} - \frac{dm_{In}}{\rho_{In}}\right)$$

therefore,

$$m_{Ga2} - m_{Ga1} = -\rho_{Ga}\frac{dm_{In}}{\rho_{In}}$$

and if we divide by V:

$$\Delta\rho_{Ga} = -\rho_{Ga}\frac{\Delta\rho_{In}}{\rho_{In}}.$$

With equation (2):

$$\Delta I_2 = \Delta I_{In} + \Delta I_{Ga}$$

$$= I_0\left(\left(\frac{\mu}{\rho}\right)_{In}\Delta\rho_{In} - \left(\frac{\mu}{\rho}\right)_{Ga}\rho_{Ga}\frac{\Delta\rho_{In}}{\rho_{In}}\right)d. \qquad \text{(A3)}$$

In reference case 1 [Fig. 6(e)], we have one fringe. There are three cases no. 2: Figs. 2(c), 5(e), (f) and 6(a), (b). All figures can be classified into segregation systems. The first one, Fig. 2(c) has four fringes, defined case no. 2a, and the second covers all the other figures and has five fringes, defined case no. 2b. Therefore, the radiation intensity change either:

$$\text{case no. 2a}: \Delta I_2 = 4\Delta I_1,$$

and

$$\text{case no. 2b}: \Delta I_2 = 5\Delta I_1$$

or, from equation (1):

$$\text{case no. 2a}: \Delta I_2/dI_0 = 4\Delta I_1/dI_0$$

$$\text{case no. 2b}: \Delta I_2/dI_0 = 5\Delta I_1/dI_0.$$

For case no. 2a and from equation (3) we gather:

$$\Delta\rho_{In} = \frac{4\Delta I_1/dI_0}{\left(\frac{\mu}{\rho}\right)_{In} - \left(\frac{\mu}{\rho}\right)_{Ga}\frac{\rho_{Ga}}{\rho_{In}}} = 8.3 \text{ kg m}^{-3}$$

and similarly for case no. 2b we calculate $\Delta\rho_{In} = 10.7$ kg m^{-3} and eventually

$$\text{case no. 2a}: \Delta C = \frac{\Delta\rho_{In}}{\rho_{Ga}} = 1.4\times10^{-3} \quad \text{or}$$

0.14 w% indium change;

$$\text{case no. 2a}: \Delta C = \frac{\Delta\rho_{In}}{\rho_{Ga}} = 1.8\times10^{-3} \quad \text{or}$$

0.18 w% indium change.